

Numerical simulation of respiratory flow patterns within human lung

R.K. Calay *, Jutarat Kurujareon ¹, Arne Erik Holdø

CFD Research Group, Faculty of Engineering and Information Sciences, University of Hertfordshire, Hertfordshire, UK

Accepted 24 October 2001

Abstract

A computational fluid dynamics (CFD) modelling approach is used to study the unsteady respiratory airflow dynamics within a human lung. The three-dimensional asymmetric bifurcation model of the central airway based on the morphological data given by Horsfield et al. (J. Appl. Physiol. 67 (1971) 207) was used in the present study to simulate the oscillatory respiratory. The single bifurcation was found to be sufficient to give a number of results which both qualitatively and quantitatively agreed well with other published experimental and CFD results. Numerical simulation were made for two breathing conditions: (a) resting or normal breathing condition and (b) maximal exercise condition. The respiratory flow results for the both conditions are found strongly dependent on the convective effect and the viscous effect with some contribution of the unsteadiness effect. The secondary motions were stronger for the normal breathing condition as compared with the maximal exercise condition. The difference between the two cases is the flow separation regions found close to the carinal ridge for maximal exercise condition. For normal breathing condition no separation regions was observed in this region. © 2002 Elsevier Science B.V. All rights reserved.

Keywords: Airways, airflow, modeling; Flow, Respiratory air; Lung model, asymmetric bifurcation; Mammals, airflow dynamics

1. Introduction

The respiratory diseases such as asthma, emphysema and bronchitis are connected with the air pollution in the nowadays-urban environment and the number of these diseases tends to increase. The therapy of respiratory diseases mostly uses

pharmaceuticals in the form of aerosol delivered into the lungs. The efficiency and efficacy of the therapy are also dependent on the size of the drugs particles, their transport and deposition in the lungs. Very little information on the pattern of the particle deposition or the effectiveness of the aerosol treatment is available and this forms an effective area of clinical respiratory research. However, knowledge of the airflow mechanism within the airway is the first step in the understanding of the movement of the particles and their deposition in the respiratory airflow net-

* Corresponding author. Tel.: +44-1707-284124; fax: +44-1707-285086.

E-mail address: r.k.calay@herts.ac.uk (R.K. Calay).

¹ Present address: Department of Mechanical Engineering, Ubonratchatani University, Thailand.

work. The goal to understanding the airflow mechanisms can be approached either using physical modelling or numerical modelling of the respiratory airflow network.

The airways network has quite small dimension and the smaller airways deep down into the lungs are inaccessible. It is difficult to simulate the highly asymmetric branching structure together with curvatures of the bifurcation in physical models. Research on scale models shows that it is not easy to retain dynamic similarity to the physical model. Therefore, most experimental techniques for the study of physical scale models of the airflow in the lung are limited up to the third generations. Numerical modeling or using computational fluid dynamics (CFD) offers an alternative to study the airflow employing a physically realistic model. Parametric studies for airflow patterns in the inaccessible regions and particle deposition can also easily be carried out with comparative ease. It is therefore possible to develop an insight to airflow patterns and particle transport with the CFD modelling and gain information, which will avoid inappropriate clinical trials and wasted effort. However, to correctly predict the complex respiratory flow using CFD simulations extensive computing of facilities are required.

Several studies of respiratory airflow dynamics have been performed until now. An extensive literature search is provided in Kurujareon (2000). Schroter and Sudlow (1969) made the earliest experimental study of airflow dynamics within a human respiratory network. Their test model was of a single symmetric bifurcation and flow was at Reynolds numbers (based on local diameter) ranging from 50 to 4500. They concluded that the inspiratory flows were independent on either Reynolds number and entry velocity profiles. Other experimental studies of the respiratory airflow dynamics also concluded that the respiratory flow patterns were likely dependent on the airway geometry (Chang and El Masry, 1982; Isabey and Chang, 1982; Pedley, 1977; Zhao and Lieber 1994a,b). These studies concluded that quasi-steady could be assumed for the respiratory flow. However, these investigations were based on the normal breathing condition. Most of these

experimental studies were used a simply symmetric bifurcation of the airway except for few studies (Chang and El Masry, 1982; Isabey and Chang, 1982; Menon et al., 1984) which investigated the airflow dynamics in the central airway up to the third generation of the bifurcation.

There also have been a number of studies using CFD in both two- and three-dimensional bifurcating tube models. A significant difference was found in between the flow patterns predicted by the symmetric and the asymmetric models and also between two- and three-dimensional models. The existence of separation regions occurring at the outer walls of the bifurcation (flow divider) in the two-dimensional models (Wilquem and Degrez, 1997) was not apparent in the three-dimensional model studied by Gatlin et al. (1995, 1997a). This is due to the three-dimensional effect or perhaps due to the sharp outer walls of the bifurcation as suggested by Pedley (1977). Kurujareon et al. (1997, 1998) investigated the effect of inlet boundary conditions on the numerical simulations of respiratory flow. The study used a three-dimensional model of the central airway based on the anatomic details given by Horsfield et al. (1971). The simulation was generated using time dependent oscillatory flow for the normal breathing condition. The results showed the qualitative agreement of the flow features with the experimental work given by Menon et al. (1984). It is obvious from the literature studies that many previous studies of the respiratory airflow dynamics studies are based on quasi-steady or transient-oscillatory flow at low frequencies of 0.25, 1, 2, 4 Hz equivalent to 2.25, 9, 18 and 36 in the actual airway. Considerable efforts have been devoted to identifying the conditions under which the flow can be considered to be quasi-steady. In fact the quasi-steady state can only be assumed at very low Reynolds number and low frequency. Laminar flow conditions exist only in very small airways deep down into the lung at resting condition. The respiratory flow is more dependent on oscillatory time dependent flow and the onset of turbulence is likely within the central airway region. Although there are few studies using a realistic model of the central airway, including asymmetric bifurcation and multiple generations

of the branching (Gatlin et al., 1997a,b; Wilquem and Degrez, 1997), the results are based on the assumption of the steady flow. The aim of this study is to numerically simulate the time dependent flow phenomenon within an asymmetric bifurcation model of the central airway at different breathing conditions.

2. Materials and methods

2.1. Pulmonary fluid dynamics

The airflow within the respiratory network can be described through the governing equations for fluid flow which are based on conservation laws for a physical system. The momentum equations in conjunction with the continuity equations are sufficient to describe the motion of airflow in the respiratory system. The three-dimensional incompressible conservative equations for conserved variable U can be expressed as:

$$\frac{\partial}{\partial t} \int_V U dV + \oint_S F_n dS = 0, \quad (1)$$

$$F_n = \vec{F} \cdot \vec{n},$$

where vector $U = (\rho, u, v, w, E)^T$ in which ρ the density of the fluid, u, v, w , are the Cartesian velocity components and E is the total energy per unit volume, V . The term F_n expresses flow flux entering and leaving the unit volume boundary surfaces S .

The velocities in the airway network are very low and decrease as the flow passes through the smaller airways deep down into lungs. The maximum velocity can be found in the central airway and the transition to turbulence may occur within this region under the breathing conditions other than the resting condition such as the maximum exercise. The maximum velocity found in any case yields the Mach numbers (M) of no more than 0.1. Hence the compressibility effect can be neglected under the condition that $\Delta\rho/\rho_0 = \frac{1}{2}M^2 \ll 1$ (White, 1991). The air is a Newtonian fluid and the dynamic viscosity μ is independent of the rate of shear. Therefore, the airflow in the respiratory system can be treated

as an incompressible, viscous flow. The respiratory airflow is a periodic function varying with respect to time, therefore the transient simulations should be performed to take the effects of unsteady flow into account. Pure oscillatory flow of an incompressible fluid at a particular location in the lungs can be characterised by dimensionless frequency or Womersley number squared ($\alpha^2 = a^2\omega/\nu$) and dimensionless Stroke length, L/a . In each generation of the conducting airway, normal breathing falls in the range of relatively low frequency ($0.01 < \alpha < 3$) and large amplitude ($100 < L/a < 2,000$). The frequencies, 0.2 and 0.8 used in the present simulation are significantly below the natural frequency of the model ($f < a/L$ ($= 331/0.15 \sim 2$ kHz)).

2.2. Grid model construction

In the present study the models were constructed based on the anatomy 'Model 1:zone1' given by Horsfield et al. (1971), which represents the central bronchi down to the lobar bronchi. This model provided realistic details of the asymmetry of branching geometry, angle, radii of curvature and flow rate distribution which are the important parameters in the flow field. The flow distribution in each branch is modelled with the restrict assumption that all the alveolar duct systems are similar and there are no regional differences in effective compliance.

The details of airway lengths, diameters, branching angle and the ratio of curvature radius (R) to daughter diameter (d) together with the airflow rate distributions at resting condition in each branch are given in Table 1. The outer walls of two daughter branches do not make sudden angled divergence from the corresponding walls to the parent tube. Rather they curve away to a new line direction. At a bifurcation (flow divider), where any pair of daughter branches forms the carina at the parent bifurcation, the changing cross-sectional shape of the bifurcation was made to agree with the ratio of axial curvature to the daughter branch airway diameter. The cross-sectional shape of the bifurcation from the parent tube to daughter tubes also change.

2.2.1. Single bifurcation

For a single bifurcation model of the central airway, the model being studied here consists of a straight pipe (the trachea) and two main right and left bronchi of the branching number 0, 1 and 10 (Table 1). For the right daughter branch, branching angle (α) is 35°. For the left daughter airway, branching angle (β) is 73°. The parent tube has circular cross-section until it reaches the onset of transitional zone. The tube then flattens, holding the cross-sectional area constant while laterally expanding into an elliptically shaped region. Within the final portion of the parent tube there is a complex curved carina region, with the onset of daughter branches located at the carinal centre point. Surfaces in this area provide for smooth interfaces between the primary tube and the subsequent branches. The carinal ridge was made sharp to ease the modelling problem. It was justified because in general the ratio of carinal ridge radius to the branch radius (r/d ; where r is the curvature radius at the carinal ridge and d the diameter of each daughter branch) is approximately 0.1 or less. This indicates that at the centre of the flow divider the leading edge is relatively sharp. Each daughter branch is circular at its onset. The curvature of the daughter branches proceeds through to the branch angle.

The model consists of 84 blocks with structured hexahedral grid cells to ease the geometry and grid generation. In the circular cross-sectional plane, there are 12 numerical blocks equally dis-

tributed through the model. In order to capture the high velocity gradient present next to the walls, the grid needed to be graded towards the wall. Particularly at the vicinity of bifurcation (the flow divider) the grid is made finer than the elsewhere to capture the high velocity gradient and pressure drop, which may occur in this region.

2.2.2. Multiple bifurcation

The results of single bifurcation were compared with the results of multiple-bifurcation model by Jolliffe (2000). The model was based on same physiological details and same computational method was used. It consists of the trachea; two main right and left bronchi; upper, middle and lower right lobar bronchi, and upper and lower left lobar bronchus of the branching number 0, 2, 6, 11, 14 and 15 (see Table 1). The model dimensions of the multiple-bifurcation model are also summarised in the Table 1.

Having established the geometry and dimensions of bifurcation models the numerical grid models were generated using a grid generator package 'Gridgen'. 'Gridgen' is commercial software that generates computational meshes from engineering drawings. The model was split into 12 blocks equally distributed through the model and there are 12 blocks in the cross-sectional plane of the tube throughout the model. The mesh lines were smoothed out towards the walls to capture high velocity gradients close to the walls. The

Table 1
Geometric details and flow distribution in the central airway

Branch	Diameter (mm)	Length (mm)	Branching angle (°)	R/d	Flow (% of trachea)
0 (trachea)	16.0	100.00	0	0	100.00
1 (left)	12.0	50.00	73	4.5	45.0342
2 (upper left)	7.5	16.00	48	3.5	18.9193
6 (lower left)	8.0	11.00	44	6.3	26.1149
10 (right)	11.1	22.00	35	3.0	54.9658
11 (upper right)	7.3	15.60	63	1.7	18.9193
13 (right)	8.9	26.00	15	2.3	36.0456
14 (middle right)	5.2	21.00	61	8.0	9.9316
15 (lower right)	6.4	8.00	15	5.9	26.1149

Note: Dimensions given here pertain to 75% TLC and each branch has identification corresponding to that given by (Horsfield et al., 1971).

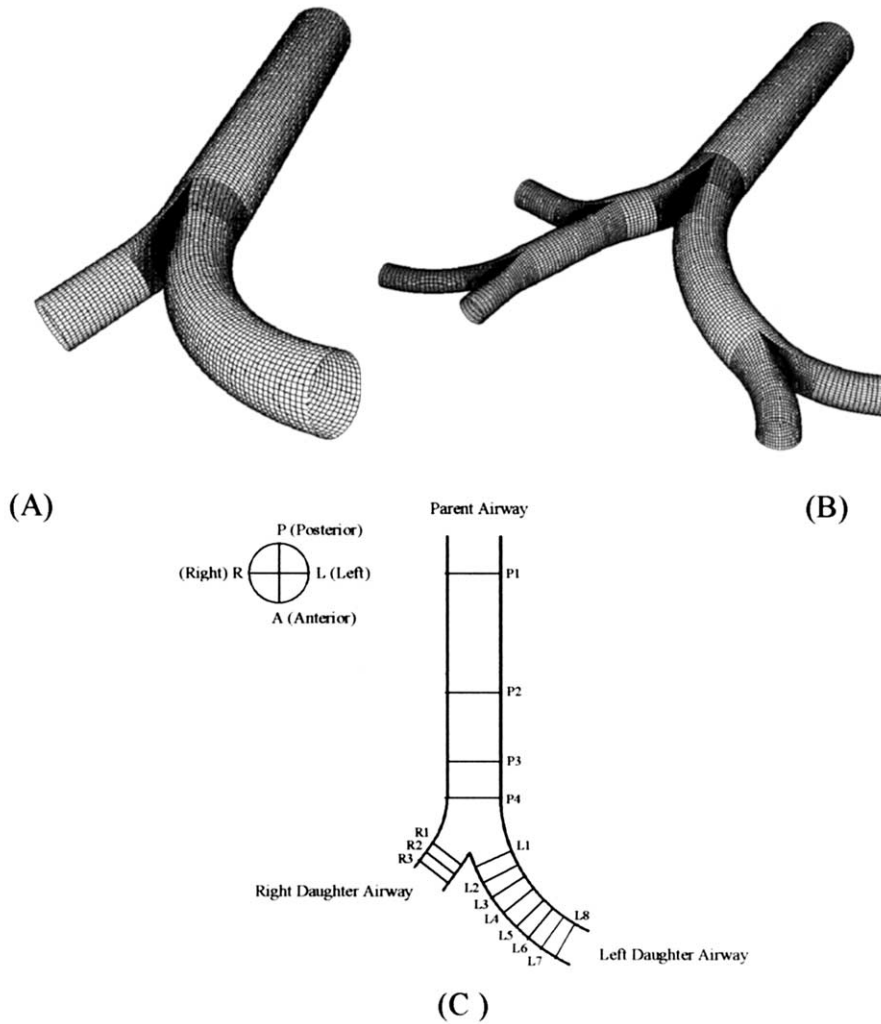


Fig. 1. Three-dimensional mesh model used for numerical simulation of flow in a lung model: (A) An asymmetric single bifurcation; (B) a multiple bifurcation; (C) 15 stations and two bifurcation planes, R–L and A–P for the single bifurcation model where results are taken.

resulting grid models are illustrated in Fig. 1A and B.

2.3. Solution of flow equations

The governing equations (Eq. (1)) are discretised in space using cell-centre finite volume method on a conventional structured mesh. The discretisation is performed on the conservative form of the governing equations so that the discretised equations remain conservative. The grid

points are regarded as points distributed with unit intervals along the axis in a curvilinear coordinate system. The Cartesian coordinate is denoted by x_i , with $i = 1, 2, 3$ and the curvilinear is denoted ξ_1 .

On the computational mesh, the governing equations are applied to hexahedron cells. Consequently, (Eq. (1)) applied to the volume $V_{i,j,k}$ is approximated and replaced by:

$$V_{i,j,k} \frac{\partial}{\partial t} U_{i,j,k} + \sum_l \vec{F}_l \cdot \vec{S}_l = 0, \quad (2)$$

where $U_{i,j,k}$ is the cell average of U and \vec{F}_l is the numerically approximated flux through \vec{S}_l and the summation is over $l = (i \pm \frac{1}{2}, j, k), (i, j \pm \frac{1}{2}, k), (i, j, k \pm \frac{1}{2})$.

Numerical flux vector can be divided into two parts: convective part and diffusive part. The convective part is defined by a high order extension Roe's scheme with limiters to retain the total variation diminishing (TVD) property of the scheme (Hirsch, 1990). The diffusive numerical fluxes are calculated using interpolation and central differencing of the conservative variables. Implicit time stepping is used for stability reasons. To increase the convergence rate, local time stepping is used. The details of the numerical model is described elsewhere (Kurujareon, 2000).

2.3.1. Concurrent block jacobi (CBJ) method

A large number of nodes are required to solve the flow problem numerically where the use of parallel multi-block solver proves to be useful. A parallelised CFD solver based on CBJ with an implicit numerical scheme (Jenssen, 1992) was employed. The matrix for each multi-block is solved separately therefore the use of parallel processors can be made to solve large computational problem, efficiently with the aggregate power of many computers. In this study 84 blocks were used and implicit scheme for solving flow equations was used inside each block to accelerate convergence rate especially where large time scale was present. The explicit coupling at the interfaces of the blocks was used by means of line relaxation procedure based on Gauss–Seidel method.

2.3.2. Numerical boundary conditions

Numerical models always represent a truncated lung model for computing reasons. Therefore, appropriate boundary conditions for the flow domain becomes important. The choices of boundaries for domains possessing multiple inflow/outflow boundaries with time dependent conditions are not obvious. The lack of information of the time dependent pressure variation in the lungs prevents the use of pressure boundary condition. In this case the resulting mass flow will not be known at the first stage and will require the use of a further control loop in order obtain

the correct flow rate into the domain. However, many researchers have used pressure boundary condition for the respiratory flow modelling (Gatlin et al., 1995, 1997a,b). The only known physiological information, which can be used as boundary condition in the numerical simulation of flow is the variation of tidal volume (VT) of air entering the mouth during the respiratory cycle as measured by a spirometer. This led us to use a velocity boundary condition on the inflow/outflow boundary. It may be assumed that the volume distal to the respiratory bronchioles is the same throughout the lungs and that change in volume is the same everywhere. The airflow rate in a given airway can be apportioned according to the number of respiratory bronchioles that it serves, with the trachea flow rate of 100% of the flow rate. The uniform velocity boundary conditions applied to the inflow/outflow boundary vary with time as a sinusoidal time function. The control of flow rates in right and left daughter airways was regulated to be 55 and 45% of the flow rate in the trachea, respectively.

The airway walls are covered by the cilia and the walls of central airways are corrugated with cartilage rings. They are normally lined with layer of mucus, which tends to make them smooth. In addition, in the region of the central airways the flexibility of the airways can be neglected. The airways up to this point are all of large diameter and such as are found not to expand (in both length and diameter) by a considerable amount during the breathing cycle.

Therefore, the models studied here are assumed to be smooth wall surfaces and solid walls, hence no-slip boundary condition was applied to the airway walls. The fluid is assumed to be homogeneous, incompressible and Newtonian. The air density, ρ_{air} is 1.225 kg m^{-3} and viscosity $\mu_{\text{air}} = 1.79\text{E-}7 \text{ Pa s}^{-1}$. For normal breathing condition a laminar model was selected. For the maximal exercise breathing condition peak Reynolds number is 4.6×10^4 , which means flow is turbulent therefore requires model for turbulence. Large eddy simulation (LES) was used for maximum exercise breathing condition.

A series of validation studies have been undertaken and the results showed that the computa-

tional model is robust and capable of estimating unsteady respiratory flow in a lung model (Kuru-jareon, 2000). Numerical simulations were made for two complete cycles of respiration for each breathing condition. Numerical time of 200 and 2000 time steps were selected to complete two respiratory cycles. Due to the solution convergence reason, the number of time steps used for the maximal exercise condition was much greater as compared with the resting condition. The residual tolerance for termination of iteration was 1×10^{-3} . The solution was converged at every time step and results were recorded at every time step. Table 2 lists the respiratory flow parameters investigated in this study.

Table 2
Respiratory flow parameters for each respiratory condition

Parameter	Resting condition	Maximum exercise condition
Tidal volume, V_T (L)	0.5	3.33
Breathing frequency, f (Hz)	0.2	0.8
Time Period, T (sec/cycle)	5	1.25
Time increment, Δt (sec)	0.05	0.00125
$t^* = 4v \Delta t/D^2$	0.01	2.78×10^{-4}
Maximum mean velocity at the trachea, \bar{U}_{\max} (mm/s)	1562.5	41 625
Reynolds number, Re	1.75×10^3	4.66×10^4
Womersley number, α	2.37	4.747
Dimensionless frequency, $\alpha^2 = a^2 \omega/v$	5.6169	22.534
Dean number, $Dn = Re (a/R)^{0.5}$ or $\alpha^2(L/a)(a/R)^{1/2}$	664.24 (parent)	17 634.91 (parent)
	290.73 (right)	7745.27 (right)
	195.06 (left)	5179.07 (left)
$L/a (= 1/St)$	310.85	2070.25
a/R	0.142 (parent)	0.142 (parent)
	0.166 (right)	0.166 (right)
	0.111 (left)	0.111 (left)

2.4. Grid sensitivity studies

Grid sensitivity study was carried out to ensure that the results are insensitive to the size of grid. Only the inspiratory flow was used for investigating the grid independent for single bifurcation model for a steady flow because the inspiratory flow is more prone to the onset of turbulence compared to the expiratory flow. Four different grid sizes with 31 104, 79 820, 159 872 and 320 980 nodes were studied at the maximum inspiratory peak flow rate under resting condition. At this stage, only the peak velocity during inspiration was used to ensure that the results at the highest Reynolds number were independent of the grid size.

A uniformly distributed velocity profile was imposed at the inlet of the parent tube with an average value of 1562.5 mm s^{-1} corresponding to Reynolds number of 1.57×10^3 based on parent airway diameter (16 mm). The axial velocity profiles were taken from at different cross sections in the parent airway and daughter airways. Fig. 1C shows the 15 cross-sectional stations in the parent and daughter airways. Stations P1, P2, P3 and P4 are located in parent airway. P1 and P2 are at 1 local diameter and 3 local diameters from the inflow/outflow boundary in parent airway. P3 and P4 are located at $1\frac{1}{2}$ local diameters and 1 local diameter from the carina in parent airway. L1, L2, L3, L4, L5, L6 and L7 are located in left daughter airway at every $\frac{1}{2}$ local diameter from the carinal ridge and L8 is located at $\frac{1}{2}$ diameter from the inflow/outflow boundary. R1 and R2 are located at every $\frac{1}{2}$ diameter from the carinal ridge in right daughter airway and R3 at $\frac{1}{2}$ diameter from the inflow/outflow boundary. The axial velocities were obtained from two planes to the model. Plane R–L (right–left) is the same plane as the bifurcation from right to left hand sides of the model. Anterior to posterior (A–P) is the plane normal to the bifurcation plane from anterior to posterior of the model.

The results at P1 and L3 of four different grid sizes were compared. At station P1, one diameter from the inflow boundary in the parent tube, the velocity profiles both in the bifurcation and normal plane to the bifurcation for all grid sizes

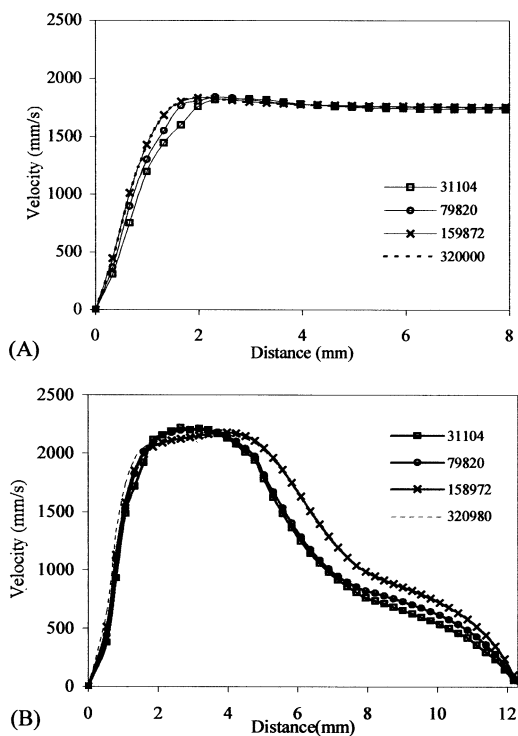


Fig. 2. Axial velocity profiles in the R–L plane for four different mesh sizes: (A) at the station (P1) 1-diameter from the inlet in the parent airway; (B) at the station t (L8) 1-diameter from the outlet in left daughter airway.

yielded the similar results at the centre of the pipe. But in the region near the walls the velocity profiles in each grid model were noticeably different. This region being within the boundary layer thickness is most influenced by the grid size.

Comparing between four grid sizes, the velocity profiles near the wall for the grids 3 and 4 with 159 872 and 320 980 nodes, respectively were identical (Fig. 2). Velocity profiles in the boundary layer region obtained from these two cases were smoother than those found with coarser grids 1 and 2 with 31 104 and 79 920 nodes, respectively. The boundary layer regions observed from the grid sizes of 320 980 and 159 872 were well defined and distinct than those observed from the grids 1 and 2. This indicates that the higher number of grid cells within the boundary layer region can capture

the flow field in more detail than those for the coarser grid size cases.

The difference observed in velocity profiles near the wall between the coarse grid case and the fine grid become more noticeable as the flow develops downstream through station P2 and P3. However, the velocity profiles for the grids 3 and 4 were still similar when the flow developed downstream. It is suggested that the flow-field results obtained from the grid size of 320 980 and 159 872 node points were grid independent. A similar difference is observed in the velocity profiles in the two daughter airways near the walls between coarse grid and fine grid. The velocity profiles at the core of the flow were also different in both bifurcation plane and normal plane to the bifurcation. Particularly, at the inner walls of the bifurcation in both daughter airways, the axial velocity profiles in bifurcation were significantly different. The skewed velocity profiles were found towards the inner wall of the bifurcation (outer wall of the bend) for all grid sizes investigated. The skewed or distorted axial velocity profiles in both daughter airways were due to the secondary motions.

The axial profiles were found to be less distorted for coarser grid (models 1 and 2) than for the finer grid (models 3 and 4). This can be due to fact that the higher grid resolution is able to resolve more detail of the secondary vortices than the coarser grid resolution or to capture the accurate physical feature of the flow field. Thus, the axial velocity profiles observed in the finer grid were more distorted than the coarse grid cases.

Due to high computing power and computing time requirements, the optimum grid size is always sought. For the present study results from the grid 3 with 159 872 nodes were assumed to be grid independent and was chosen for further simulations. Although the velocity profiles obtained from all grid sizes as shown in Fig. 2, seem to be different yet the difference in the results obtained from the grids 3 and 4 was only up to 1–2%. It was clearly seen that the change from grid sizes of 159 872–320 980 nodes yielded similar results that can capture the flow field in more detail when compared with the results from coarser grids.

3. Results

Fig. 3 presents a comparison between the simulations using single bifurcation model and multiple-bifurcation model. Velocity profiles at selected stations in the parent and daughter airways are compared for normal breathing case.

The comparison between the single bifurcation and multiple bifurcations was made only for the resting condition. Fig. 3 shows the similarities and

differences in the velocity profiles at different stations for the two models. The presented velocity profiles in other figures are normalised by the maximum average velocity in each branch for the respiratory flow and the non-dimensional diameter is normalised by the local diameter.

The velocity profiles in the bifurcation plane (R–L) and in the plane normal to the bifurcation (A–P) are also different to one another. This difference can be clearly observed in the profiles

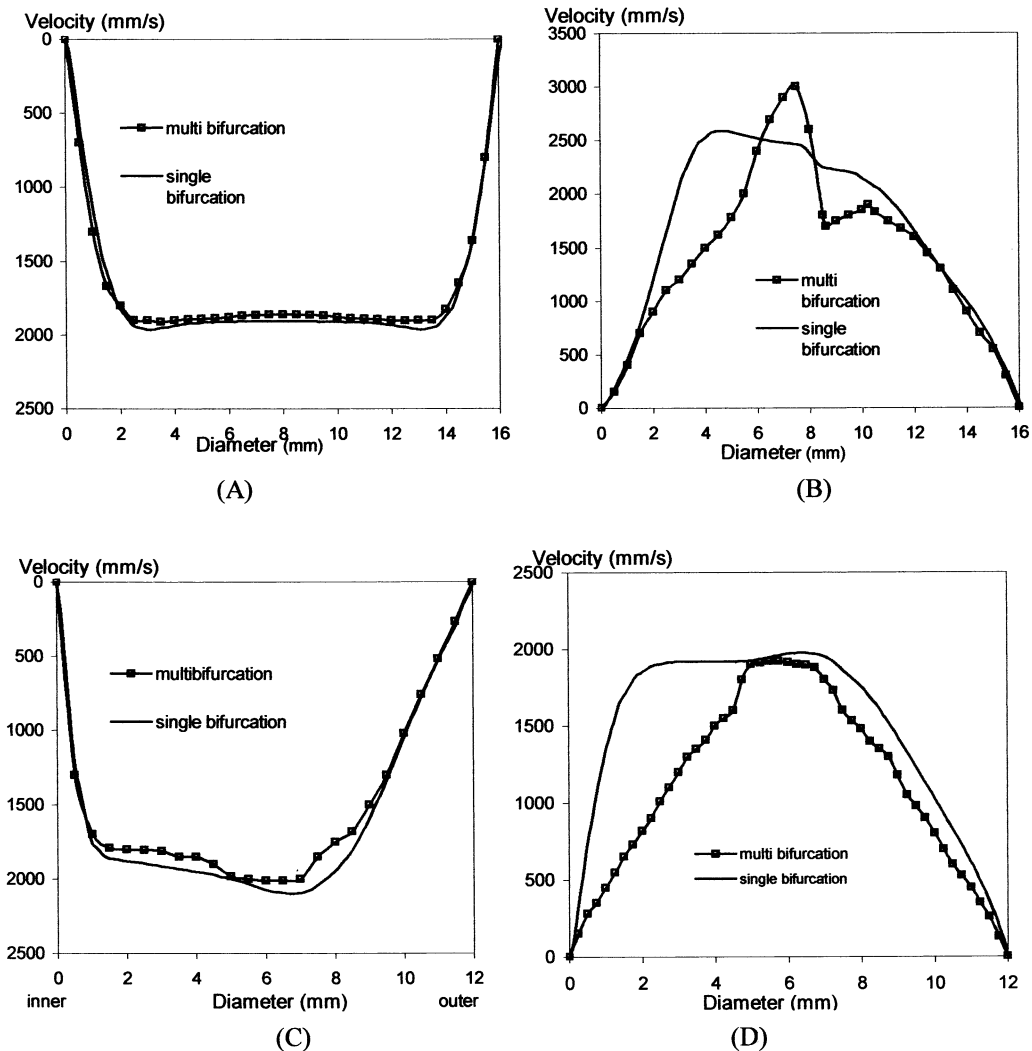


Fig. 3. Axial velocity profiles in the A–P plane for normal breathing ($Re = 1.75 \times 10^3$, $\alpha = 2.37$): (A) at station P1 for maximum inspiration; (B) at station P4 for maximum expiration; (C) at station L3 for maximum inspiration; (D) at station L1 for maximum expiration.

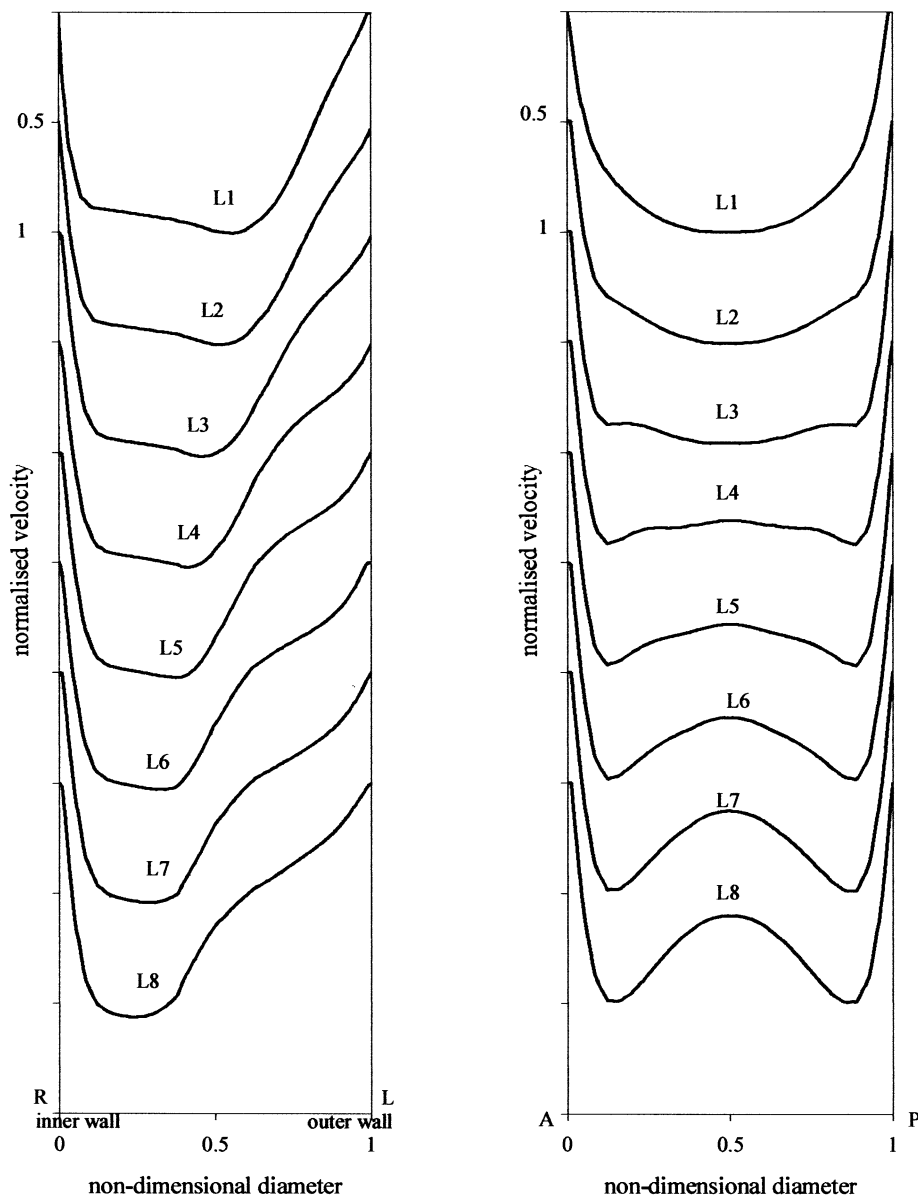


Fig. 4. Comparison of axial velocity profiles in the left daughter airway for resting condition ($Re = 1.75 \times 10^3$, $\alpha = 2.37$): (A) R–L plane; (B) A–P plane.

shown in Figs. 4 and 5. A comparison of the flow features for resting condition and maximal exercise condition is shown in Fig. 6. Figs. 7–9 quantitatively highlight the differences in the velocity profiles.

Differences in the flow characteristics during

accelerating and decelerating can be observed in velocity profiles for resting breathing condition presented in Fig. 10. The results for expiration were independent of initial conditions i.e. the results obtained from the first and second expiration phases were identical. But the results at the

beginning of the first inspiration phase and second inspiration phase (at $T = \pi/10$, $21\pi/10$) were different. This is due to a different numerical initial condition at the first time step of the inspiration phases. At time $T = 0$, at the beginning of the first inspiration phase a uniform velocity is imposed at the inlet. Whereas for the second inspiration phase (at $T = 2\pi$) velocity boundary condition is

due to the end of the first expiration phase. However, this difference in the inspiration phase disappeared after the first four time steps. The results were reproducible thereafter between any two cycles. Therefore, the simulations were performed just for two cycles for the resting condition and 1.5 cycles for the maximal exercise condition to save computing time.

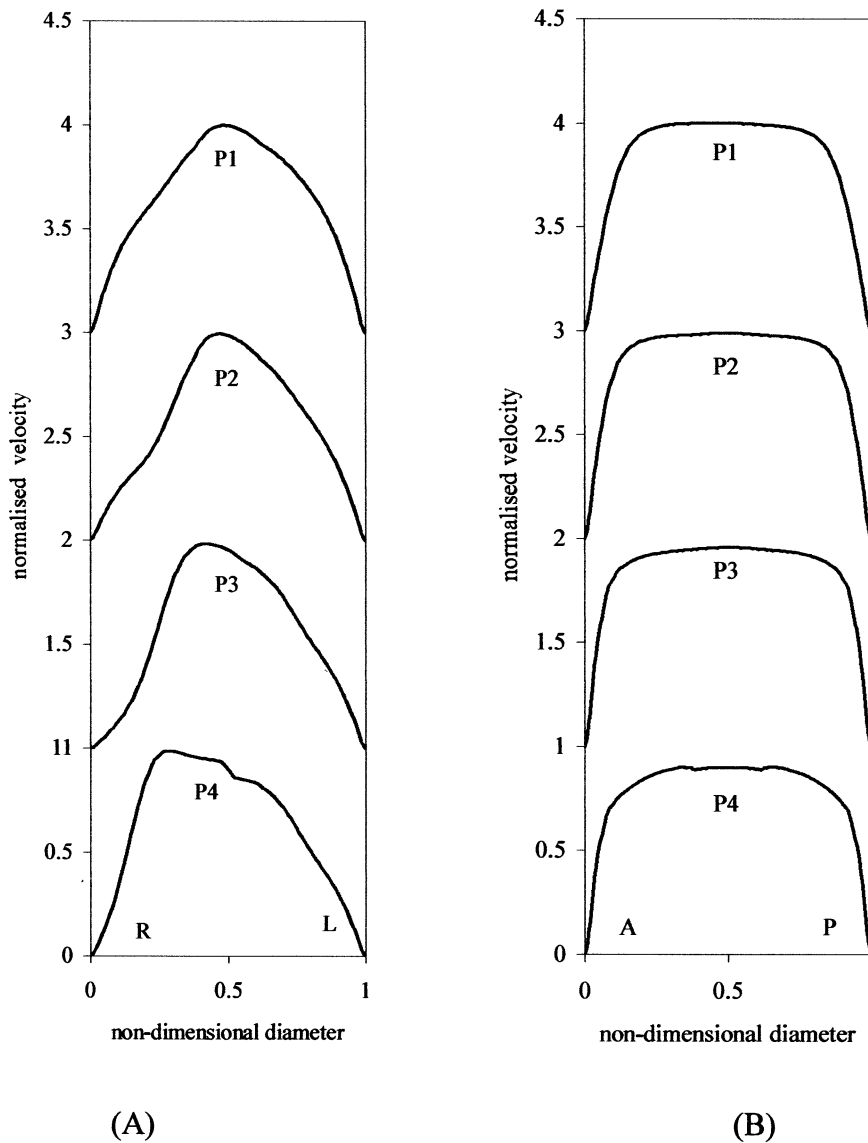
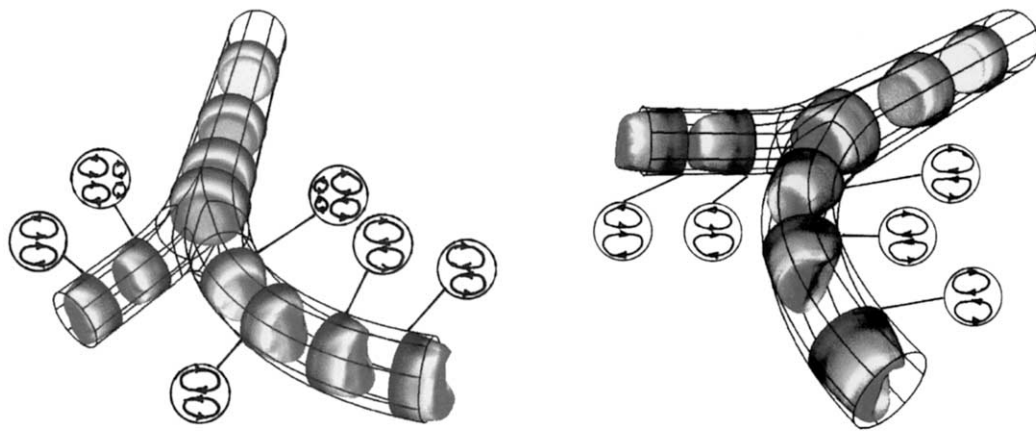


Fig. 5. Comparison of axial velocity profiles in the parent airway for resting condition ($Re = 1.75 \times 10^3$, $\alpha = 2.37$): (A) R–L plane; (B) A–P plane.



(A) Peak inspiratory flow for the maximal exercise condition (B) Peak inspiratory flow for the resting condition

Fig. 6. Comparison of flow features for resting condition ($Re = 1.75 \times 10^3$, $\alpha = 2.37$) and for the maximal exercise condition ($Re = 4.66 \times 10^4$, $\alpha = 4.747$) for maximum expiration.

4. Discussion

4.1. Single bifurcation vs. multiple bifurcation model

A good agreement was observed between the velocity profiles for the single bifurcation and multiple bifurcation models. Particularly within the boundary layer where the mesh cells in both models are graded towards the wall. Some differences in velocity profiles are seen at the centre region near of the tube (Fig. 3). These differences in velocity profiles are likely to be caused by the poorly graded mesh in this region of the multiple bifurcation model. The mesh density in the centre is large but the cell size abruptly increases towards the airway walls before it becomes very fine again close to the walls.

Similar agreement was found between the axial velocity profiles of the two models in the bifurcation plane in the daughter airways. The velocity profiles obtained were qualitatively similar but differences were found at the region near the centre of the tube. The velocity profiles obtained from the single bifurcation model were more distorted than those obtained from the multiple bifurcation model. This is likely due to the

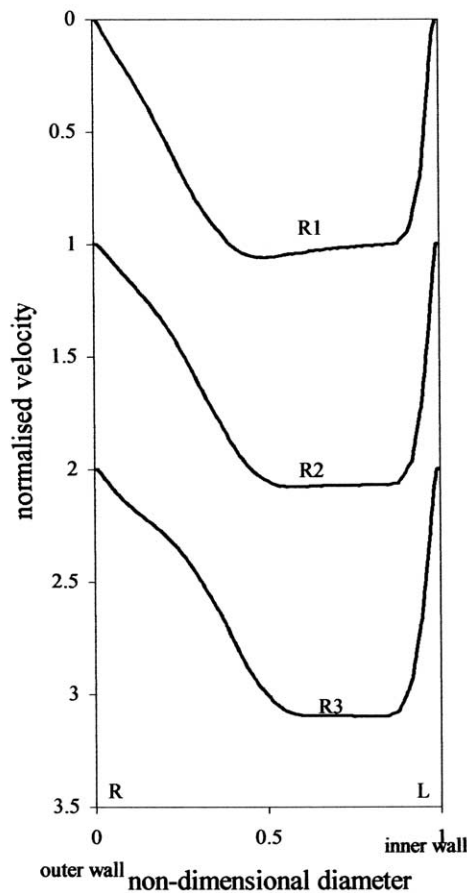
increased influence of secondary motions in the single bifurcation model. This could partly be due to inadequate grid grading in the central region of the tube for the multiple bifurcation model.

The difference in the two models was more significant for expiration phase as can be observed in the velocity profiles at stations P4 and L1 (Fig. 3B and D). The inlet velocity profile entering at the inflow boundary in the left daughter airway is a uniform velocity profile for the single bifurcation model. The inlet velocity profile at the entrance of the main left daughter airway for the multiple bifurcation case is a profile due to the two merging flow streams from the previous smaller airways (lower and upper lobar bronchi). When the flow develops downstream through the left daughter airway, the differences in velocity profiles between the single bifurcation and the multiple bifurcation cases are found. The profiles found in the multiple bifurcation models were more skewed than the single bifurcation model. The axial velocity profiles for the multiple bifurcation model were more distorted by the secondary motion caused by, firstly, the curvature of the left daughter airway and secondly, due to the merging flows from the two previous smaller airways. Whereas, only the secondary motion due to the

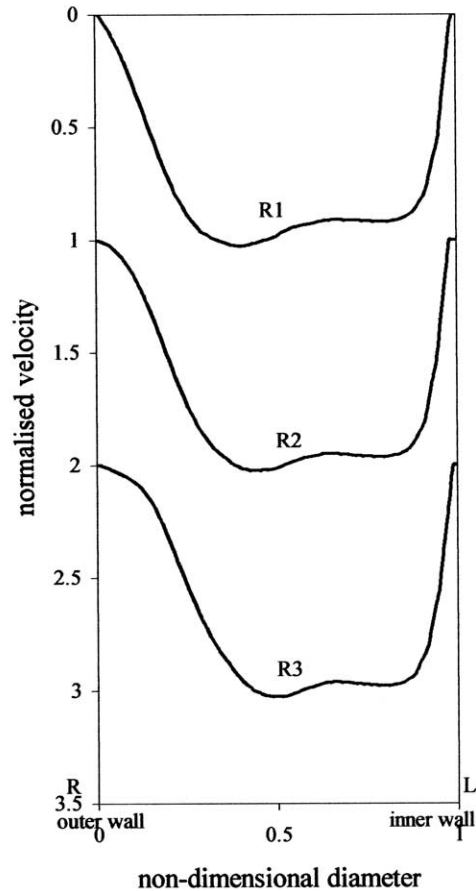
curvature of the left daughter airway distorts the velocity profile in the single bifurcation model. However, when the flow moves further downstream, the velocity profiles for those two cases tend to develop in a same flow pattern in the parent airway at stations P2 and P1. The boundary layer thickness in each model is likely to develop to a similar pattern to that seen at station P4. When the flow enters the airway, the axial velocity profiles between the two models are

different at the centre of the airway but the velocity profiles within the boundary layer region are similar.

Similar trend was observed for the axial velocity profiles in the normal plane to the bifurcation for both models. However, the velocity at the centre region of the tube for the multiple bifurcation model is significantly high from the flat profile found in the single bifurcation model. The axial velocity profiles (both in the bifurcation

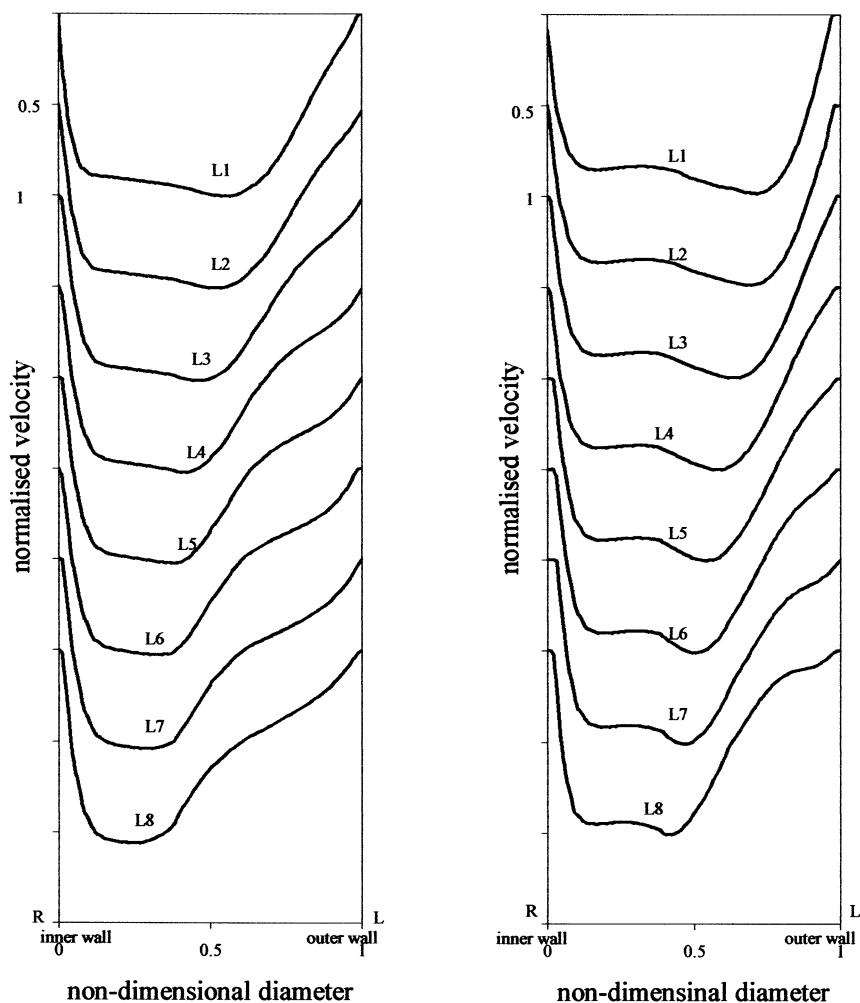


(A) Resting condition
($Re=1.75 \times 10^3$, $\alpha=2.37$)



(B) Maximal exercise condition
($Re=4.66 \times 10^4$, $\alpha=4.747$)

Fig. 7. Comparison of axial velocity profiles in the bifurcation plane in the right airway at peak inspiration for resting condition and maximal exercise condition.



(A) Resting condition

(B) Maximal exercise condition

($Re = 1.75 \times 10^3$, $\alpha = 2.37$) ($Re = 4.66 \times 10^4$, $\alpha = 4.747$)

Fig. 8. Comparison of axial velocity profiles in the bifurcation plane in the left airway at peak inspiration for resting condition and maximal exercise condition.

plane and the normal plane to the bifurcation) obtained from both models are in good agreement for the boundary layer region, but the significant differences in the profiles are found in the core of the tube.

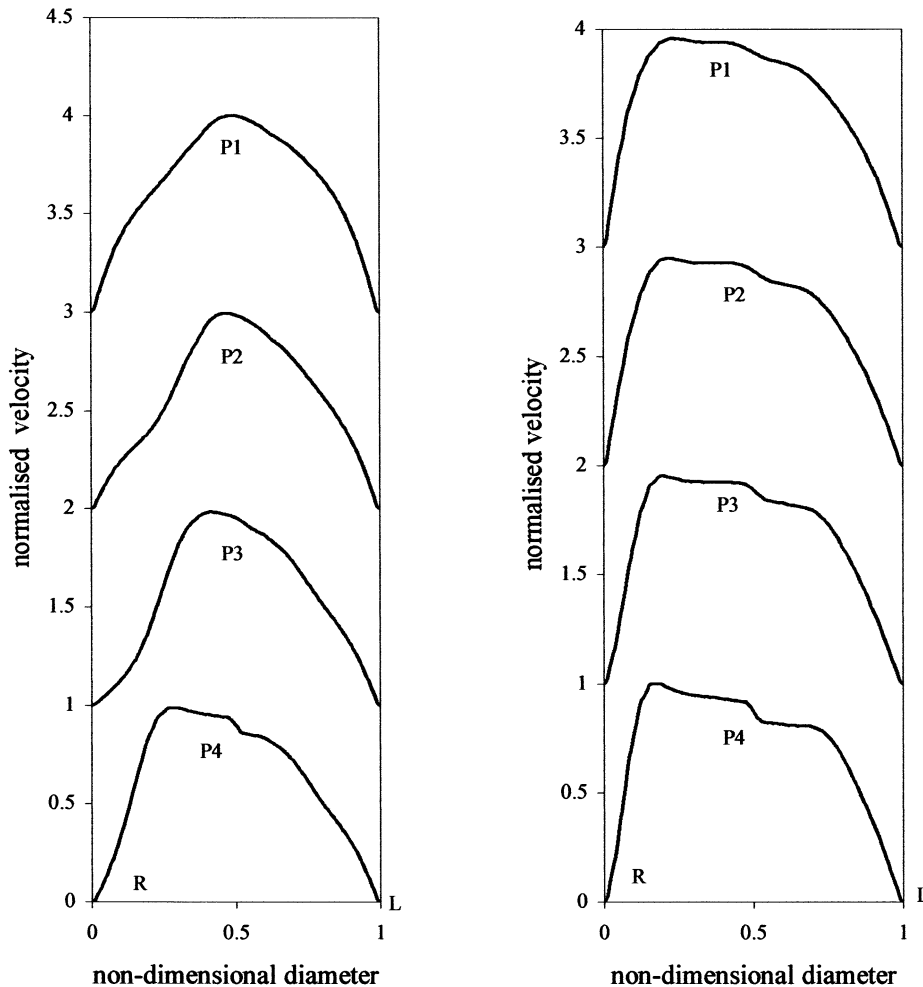
4.2. Inspiration phase

It can be seen how the flow develops as it passes through various stations down the parent airway to the two daughter airways for inspira-

tion and vice-versa for the expiration phase in Figs. 4 and 5.

The velocity at P1 is still uniform and it develops downstream as it passes stations P2 and P4 with a thicker boundary layer. Initially the peak velocity is found near the wall due to the diffusion of momentum over the cross-section while the flow tends to adjust itself during the oscillatory period

but further downstream flow develops to a profile with parabolic characteristics. However, the flow is still not fully developed when it reaches the carinal ridge (at 6.25 local diameter). The dimensionless time, t^* at this stage is 0.25 while the dimensionless time that allows the flow to be fully developed during startup flow in a short straight pipe is equal to one (Anderson and Kristoffersen, 1989).



(A) Resting condition

($Re = 1.75 \times 10^3$, $\alpha = 2.37$)

(B) Maximal exercise condition

($Re = 4.66 \times 10^4$, $\alpha = 4.747$)

Fig. 9. Comparison of axial velocity profiles in the bifurcation plane in the parent airway at peak expiration for resting condition and for maximal exercise condition.

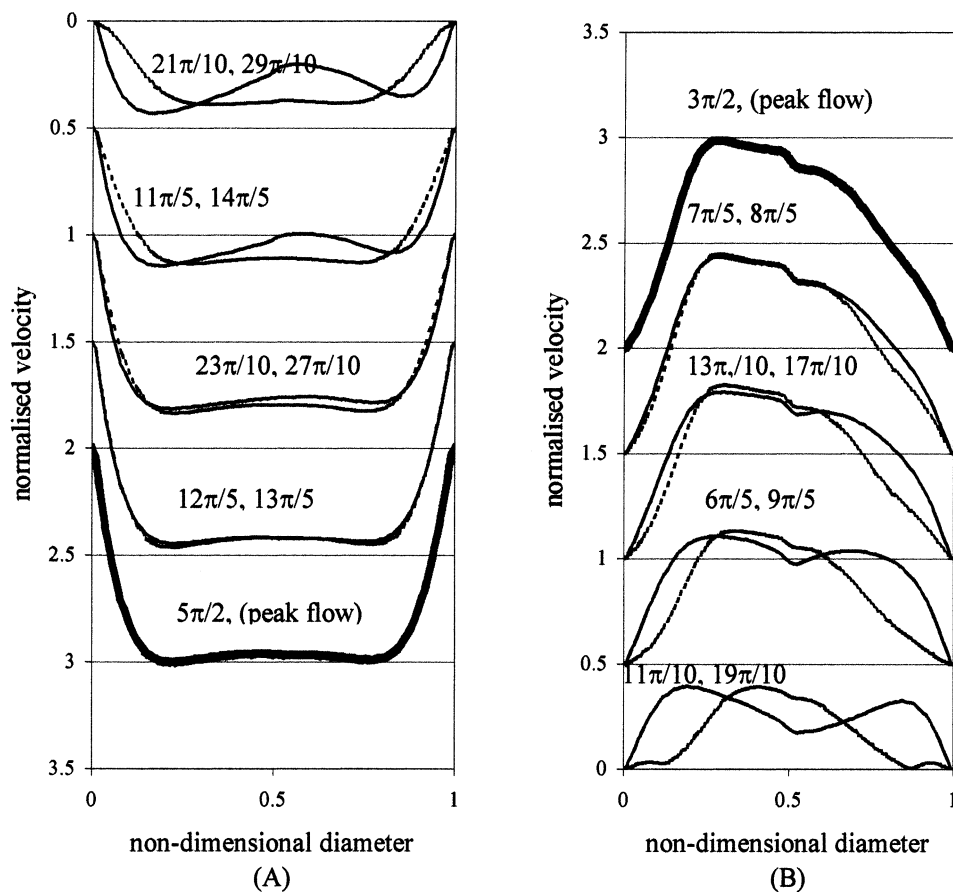


Fig. 10. Axial velocity profiles at station P4 for selected phases for resting condition ($Re = 1.75 \times 10^3$, $\alpha = 2.37$). Solid line (—) represents the acceleration; dotted line (---) represents the deceleration: (A) inspiration phase; (B) expiration phase.

At the carina the flow splits into two daughter airways. When fluid element enters the curved section at the bifurcation its path changes direction due to the curvature; the secondary motions are caused by the centrifugal force due to the curvature of the curved portion of the airway. Thus, its velocity must increase for the angular momentum to be conserved. The fluid elements on the inner wall of the curvature experience a greater change in path curvature and their velocities grow faster than the velocity on the outer wall of the curvature. A pair of vortices was found in each daughter airway, which gave rise to the distortion on the primary axial flow. The axial velocities in the bifurcation plane (R–L) in the both airways are skewed towards the inner wall of

the bend, whereas in the normal plane to the bifurcation (A–P) the profiles are symmetric and initially parabolic but flatten when they develop downstream. The axial velocities are more distorted as the flow develops downstream through station L1–L8, which can be observed in Fig. 4. Many researchers have studied entry flow into curved pipes and skewness of the axial velocity profiles was reported at high Dean numbers (Agarwal et al., 1978; Snyder et al., 1985). In the present simulations Dean number in the daughter airways was in the low to moderate range. It was noted that developing axial skew is accentuated by increasing Dean number and Reynolds number. When the flow develops further downstream from the carinal ridge (at station L5, ~ 3 local

diameters), it possesses a 'M' shape velocity profile (see Fig. 4). The distortion is more in the left airway than in the right airway due to the fact that flow rate (or Reynolds number) is higher in the right airway. The curved portion of the left airway is also longer than that in the right daughter airway.

4.3. Expiration phase

In the expiration the flow was regulated from two daughter airways by applying uniform velocity profiles at the inflow boundaries. In the right daughter airway when the flow reaches the bifurcation the velocity profile is still flat and the secondary motions were not significant. This is because the flow does not fully develop through the short straight pipe geometry of the right airway. However, in the left daughter airway axial uniform inlet velocity in the bifurcation plane (R–L) develops downstream and the velocity profile becomes skewed towards the inner wall of the bifurcation from station L3 and it becomes more skewed as flow reaches the bifurcation (station L1). When two streams from both daughter airways enter the bifurcation, these merge together in the parent tube. Due to the unequal flow rates just above the carinal ridge two pairs of unequal vortices are formed. However, these helical motions become less noticeable when flow moves downstream through the straight section of parent airway. The velocity profiles in the bifurcation plane (R–L) are skewed, which becomes symmetric as flow passes from P4 to P1 (Fig. 5). However, the axial velocity profiles in the normal to the bifurcation plane (A–P) are symmetric and flat.

4.4. Comparison with the maximal exercise condition

The flow-field for the maximal exercise case was qualitatively similar to that for the resting condition (Fig. 6A, B). The distortion of axial velocity profiles for the resting condition and maximal exercise condition was also similar during inspiration. However, there are some distinct differences between the resting condition case and the maxi-

mal exercise case. For the maximal exercise breathing condition, at the inner walls of the bifurcation close to the carinal ridge a second pair of vortices is found in both daughter airways. For the resting condition, these secondary vortices cannot be observed, because in the high velocity flow for the maximal exercise condition change in the momentum at the carinal ridge, which results in the additional vortices is much greater than in the resting condition. These secondary vortices are confined within a narrow boundary layer region at the inner walls of the bifurcation close to the carinal ridge. When the flow develops downstream these vortices disappear and the only secondary motion caused by the centrifugal forces due to the curvature is apparent at the outer wall of the bifurcation.

Due to the high velocity flow for the maximal exercise case, when the flow in the parent airway is split at the carina a new separated region is formed on the inside walls of the bifurcation near the carinal ridge. The occurrence of the secondary vortices near the carinal ridge for the maximal exercise condition is likely to be due to the escape of fluid particles from the main flow stream to a new boundary layer region formed at the carinal ridge. This phenomenon is similar to those occurring for flow in a bifurcation with a sharp carinal ridge (Heistracher and Hofmann, 1994), where the flow separation region was found just immediately downstream from the carina. This may relate to the effect that the flow velocity at the maximal exercise case is relatively high in comparison with the carina radius.

There are differences in the velocity profiles for two breathing conditions (see Figs. 7–9). The peak velocity profiles at the centre of the flow between these two conditions are also different. Due to the higher inertia force for the maximal exercise condition, prominent higher velocity profiles are observed at the core of the tube with lower velocity near the boundary layer at the inner wall of the bifurcation. Whereas, the velocity at the core of the tube for the resting condition cases are rather flat. The axial velocity profiles for the resting condition are more distorted by the secondary motions than for the maximal exercise case. The boundary layer thickness for the maxi-

mal exercise case is thinner than those found in the resting condition.

4.5. Transient simulations

The time dependent simulations showed the development of the flow features within the airway right from the start of the respiratory phase accelerating to the peak inspiration, decelerating to zero flow rate and then to peak expiration. Fig. 10A, B depicts the axial velocity profiles at station P4 at every time period ($T = \pi/10$ rad) over the second inspiration phase ($2\pi-3\pi$) in the respiration cycle and expiration phase ($\pi-2\pi$). The velocity profiles at the same flow rate during acceleration and deceleration are different within the same inspiration phase. The profiles during acceleration are distorted at the low flow rates i.e. when the flow accelerates from 'zero' flow at the changeover from expiration to inspiration. The distortion of axial velocity at this stage is due to the flow separation effects at the reversal flow when the flow changes direction from expiratory to inspiratory flow. As the flow rate accelerates to its peak value the difference in the velocity profiles for acceleration and deceleration begins to decrease. The velocity profile at the maximum flow rate (at time $T = 5\pi/2$) agrees with the results of steady-state studies at equivalent flow rate (or Re number). There is no flow separation at the beginning of the deceleration therefore the velocity profile is rather uniform and closely resembles the profile within the accelerating phase at the equivalent flow rate (at time $T = 12\pi/5, 13\pi/5$).

During expiration the flow at station P4 in the parent airway achieve velocity profile with a peak near the entrance from the right daughter airway during both acceleration and deceleration. $\pi/10$ rad after the 'zero' flow the velocity profile is with twin peak (at $T = 11\pi/10$), whereas the profile for the equivalent flow rate (at $T = 19\pi/10$) is qualitatively different. There is a significant increase in the boundary layer thickness when flow is decelerated after peak expiration, which is evident in the profile at $T = 19\pi/10$.

Similar effects were observed in the daughter airways during acceleration and deceleration. The velocity profiles were skewed towards the inner

walls of the bend centre for deceleration phase, which mean that the secondary motions are more significant during deceleration than acceleration.

The velocity profiles observed at peak flow rates are found to be in good agreement to the results obtained from previous studies steady or quasi-steady flow conditions. But the flow features are significantly different for the same flow rate during the acceleration and deceleration phase as observed from the transient velocity profiles within the same respiratory cycle. The axial velocity profiles during deceleration are more distorted due to the secondary motions than for the acceleration. The difference in velocity profiles at the equivalent flow rate between the acceleration and deceleration phases can only be due to the unsteadiness effect or due to taking $[\partial/\partial t]$ terms into account, which are assumed to be zero in steady-state solution. The difference in the accelerating and decelerating velocity profiles in the inspiration and expiration phase at the same Reynolds number is due to the difference in the temporal terms from the previous respiratory cycle. This effect decreases when the flow reaches its peak value where the contribution from unsteadiness or $[\partial/\partial t]$ tends to approach zero. Hence the quasi-steady flow can be assumed at only peak flow rate.

Pedley (1977) suggested that if the cycle period is greater than the time required for the unsteady (Stokes) viscous layer to reach approximately the thickness of the steady (Blasius) viscous layer the flow can be assumed to quasi-steady. Jan et al. (1989) proposed the ratio of cycle period to the time for steady boundary layer to develop as a measure of the importance of unsteadiness. They classified oscillatory flow into three regimes by whether the flow is dominated by unsteadiness, convective or viscous effects depending upon the order of magnitude of temporal, $[\partial u/\partial t]$, convective, $u[\partial u/\partial u]$ and viscous $[\partial^2 u/\partial x^2]$ terms with respect to that of the other terms. Three regimes were assumed to be limited by parametric values of Womersely number, α and Stroke length parameter, L/a (see Table 3). The flow classification in the present study based on Jan et al. criteria can be made as follows.

For Resting condition ($\alpha^2 = 5.15$, $L/a = 310.85$, $Dn = 664.24$) the flow can be classified in the Zone IIIa, which means that the flow is dominated by the convective effects and secondary effects are due to viscous terms, but only at the peak flow rates. At the other flow rates during each respiratory cycle, especially at the beginning of the acceleration the convective effects are still dominating the flow, but the secondary flow is distinctly different from the pattern at the peak flow rate. The flow characteristics fall in the category IIIb.

For the maximum exercise condition ($\alpha^2 = 22.535$, $L/a = 2070.45$, $Dn = 17\,634$) results were similar to the resting conditions. The flow is dominated by the convective and viscous effects (Zone IIIa) at the peak flow rate but for the rest of the respiratory cycle by the convective and unsteady effects (Zone IIIb).

The occurrence of turbulence for oscillatory flow relates to Re/α (Winter and Nerem, 1984) and a critical value of 780 has been suggested for transition to turbulence to occur in a straight tube. For resting condition Re/α remains below the above critical value. For maximum exercise condition the Re/α varies from 0 to ~ 9800 in the parent airway, therefore turbulence starts to develop close to the peak flow rate. The LES turbulence model was used to model any turbulence motions that are present during the respiratory phase. However, no similar pattern was found in parent or daughter airways as observed in a straight tube in which a sudden burst of turbu-

lence is found just following the peak velocity and it then decays almost completely during deceleration (Winter and Nerem, 1984). This may be due to a different geometry in the present study compared to a straight tube.

5. Conclusions

It was found that a single asymmetric bifurcation model is sufficient to give a number of results which both quantitatively and qualitatively agree well with other published experiments and CFD studies. Comparison with the results obtained from a multiple-bifurcation model showed that there was no difference in the flow features particularly for the inspiration case. For expiration case the differences are due to the 'inlet boundary conditions' at the daughter airways. Therefore, realistic inlet boundary condition for the expiration is necessary to get similar results from a single bifurcation model. The quasi-steady or steady assumption is only valid at peak flow rate that represents only a point in the respiratory cycle.

The flow under the normal and maximal exercise breathing conditions is strongly dependent on the geometry or Dean number (Dn) and Reynolds number (Re) both are the most important parameters influencing the respiratory flow. Therefore, the correct physiological model is a pre-requisite for accurate results. The ratio of Dean number between the right and left daughter airways that is an important parameters needs to be taken into account.

For normal breathing condition the flow is dominated by the convective effects but the secondary flow, which is due to the centrifugal forces caused by the curvature of the airway was also found to be strong. For the maximal exercise condition, the flow behaviour was similar to that found in the resting condition case. However, the convective effect in this case is likely to play a more significant role on the flow patterns than for the resting condition. In general the secondary motion for the maximal exercise condition is weaker than for the resting condition. But at the inner walls of the bifurcation close to the carinal

Table 3

Flow Regimes (as classified by Jan et al., 1989)	Limits for various parameters
Zone I: Unsteadiness effects	$L/a \leq 3$, $\alpha \geq 3$
Zone II: Viscous effects	$\alpha \leq 3$, α^2
Zone III: Convective	$L/a \leq 30$
Zone IIIa: Main effects Convective, Secondary effects Viscous	$L/a > 3$, $\alpha^2 \leq 10$
Zone IIIb: Main effects Convective Secondary effects Viscous	$L/a > 3$, $\alpha^2 \geq 10$

ridge the secondary vortices were observed only in the maximal exercise condition.

Jan et al. (1989) classification for oscillatory flow was based on symmetric bifurcation. This classification can be used only for the peak flow rate for the normal breathing condition in the present study, when the flow can be assumed to be quasi-steady. For other flow rates during the breathing cycle convective and unsteady effects influence the flow. The unsteadiness effects always play a significant role on the flow for the whole respiratory cycle. Therefore, the time dependent simulations should be performed to obtain flow features for the full breathing cycle.

The information on the velocity profile can be used to provide preliminary assessment of the transport of aerosol particles into the lungs. The flow velocity in the outer walls of the bifurcation zone is very low. Because, after the flow splits and exits from the bifurcation the fluid elements tend to move away from the centre of the curvature. Therefore, the inhaled particles are more likely to get deposited close to the outer walls of the daughter branches in the bifurcation zone.

Flow separates close to carina for the maximal exercise condition. Flow speed within the bifurcation region becomes very low due to the escape of the fluid particles into this separated region to conserve the flow momentum. This suggests that particle deposition may be higher within the area of the carina at higher breathing flow rates. However, other factors such as particle mass, size and shape determine the precise transportation and deposition of particles in the airways. Therefore, equations that govern particle transportation should be solved simultaneously with the fluid flow equations for better predictions.

Appendix A. Nomenclature

a	airway radius, pipe radius, m
c_0	velocity of sound, m s^{-1}
d	daughter airway diameter, m
D	parent airway diameter, pipe diameter, m
Dn	Dean number

f	frequency, Hz
\vec{F}	flux vector
Re	Reynolds number
S	surface area, m^2
St	strouhal number
t	time, sec
t^*	dimensionless time
Δt	time increment, sec
u	x-component velocity in Cartesian coordinate, m s^{-1}
U	conserved variables
\vec{U}	mean velocity, m s^{-1}
v	y-component velocity in Cartesian coordinate, m s^{-1}
\dot{V}	volume flow rate, $\text{m}^3 \text{s}^{-1}$
w	z-component velocity in Cartesian coordinate, m s^{-1}
V_T	tidal volume, m^3
α	Womersley number
ω	angular frequency, rad m^{-1}
ρ	fluid density, kg m^{-3}
μ	viscosity

References

- Agarwal, Y., Talbot, L., Gong, K., 1978. Laser anemometer study of flow development in curved pipes. *J. Fluid Mechanics* 85 (3), 497–518.
- Anderson, H.I., Kristoffersen, R., 1989. Numerical simulation of unsteady viscous flow. *Arch. Mech.* 41, 207–223.
- Chang, H.K., El Masry, O.A., 1982. A model study of flow dynamics in human central airways. Part 1 axial velocity profiles. *Respir. Physiol.* 49, 75–95.
- Gatlin, B., Cuicchi, C., Hammersley, J., Olson, D.E., Reddy, R., Burnside, G., 1995. Computational simulation of steady and oscillating flow in branching tubes. *ASME Bio-Medical. Fluids. Engineering. FED* 212, 1–8.
- Gatlin, B., Cuicchi, C., Hammersley, J., Olson, D.E., Reddy, R., Burnside, G., 1997a. Computation of converging and diverging flow through an asymmetric tubular bifurcation. *ASME FEDSM97* 3429, 1–7.
- Gatlin, B., Cuicchi, C., Hammersley, J., Olson, D.E., Reddy, R., Burnside, G., 1997b. Particle paths and wall deposition patterns in laminar flow through a bifurcation. *ASME FEDSM97* 3434, 1–7.
- Heistracher, T., Hofmann, W., 1994. Physiologically realistic models of bronchial airway bifurcation. *J. Aerosol. Sci.* 26, 497–509.

- Hirsch, C., 1990. Numerical Computation of Internal and External Flows, vol.2, Computational methods for inviscid and viscous flows, Great Britain: John Wiley and Sons Ltd.
- Horsfield, K., Dart, G., Olson, D.E., Filley, G.F., Cumming, G., 1971. Models of the human bronchial tree. *J. Appl. Physiol.* 31, 207–217.
- Isabey, D., Chang, H.K., 1982. A model study of flow dynamics in human central airways. Part II: secondary flow velocities. *Respir. Physiol.* 49, 97–113.
- Jan, D.L., Shapiro, A.H., Kamm, R.D., 1989. Some features of oscillatory flow in a model bifurcation. *J. Appl. Physiol.* 67, 147–159.
- Jenssen, C.B., 1992. The development and implementation of an implicit multiblock Navier-Stokes solver, Ph.D. Thesis, The Norwegian Institute of Technology, Norway.
- Jolliffe, A.D., 2000. Respiratory airflow dynamics, Ph.D. Thesis, University of Hertfordshire, UK.
- Kurujareon, J., Holdø, A.E., Jolliffe, A.D., Calay, R.K., 1997. Effects of Boundary Conditions for the CFD Modeling of Respiratory Flow in the Tracheobronchial Network, 9th International Conference on Biomedical Engineering, Singapore, 585–587.
- Kurujareon, J., Holdø, A.E., Calay, R.K., 1998. Effects of boundary conditions for the CFD modeling of respiratory flow in an asymmetric bifurcation. *ASME Advances in Bioengineering*, BED 39, 103–104.
- Kurujareon, J., 2000. Simulations of Airflow in the human tracheobronchial network, Ph.D. Thesis, University of Hertfordshire, UK.
- Menon, A.S., Weber, M.E., Chang, H.K., 1984. Model study of flow dynamics in human central airways. Part III: oscillatory velocity profiles. *Respir. Physiol.* 55, 255–275.
- Pedley, T.J., 1977. Pulmonary fluid dynamics. *Ann. Rev. Fluid Mech.* 9, 229–274.
- Schroter, R.C., Sudlow, M.F., 1969. Flow patterns in model of the human bronchial airways. *Respir. Physiol.* 7, 341–355.
- Snyder, B., Hammersley, J.R., Olson, D.E., 1985. The axial skew of flow in curved pipes. *J. Fluid Mechanics* 161, 281–294.
- White, F.M., 1991. Viscous Fluid Flows, 2nd Ed. McGraw-Hill, Inc, Singapore.
- Wilquem, F., Degrez, G., 1997. Numerical modeling of steady inspiratory airflow through three-generation model of the human central airways. *ASME J. Biomech. Engg.* 119, 59–65.
- Winter, D.C., Nerem, R.M., 1984. Turbulence of pulsatile flows. *Annals. Biomed. Engg.* 12, 357–369.
- Zhao, Y., Lieber, B.B., 1994a. Steady inspiratory flow in a model symmetric bifurcation. *ASME J. Biomech. Engg.* 116, 488–496.
- Zhao, Y., Lieber, B.B., 1994b. Steady expiratory flow in a model symmetric bifurcation. *ASME J. Biomech. Engg.* 116, 318–323.